HHS Public Access

Author manuscript

Acta Biomater. Author manuscript; available in PMC 2021 January 15.

Published in final edited form as:

Acta Biomater. 2020 January 15; 102: 100–113. doi:10.1016/j.actbio.2019.11.039.

A Detailed Mechanical and Microstructural Analysis of Ovine Tricuspid Valve Leaflets

William D Meador[a], **Mrudang Mathur**[b], **Gabriella P Sugerman**[a], **Tomasz Jazwiec**[c,d], **Marcin Malinowski**[c,e], **Matthew R Bersi**[f], **Tomasz A Timek**[c], **Manuel K Rausch**[a,b,g,*]

[a]Department of Biomedical Engineering, The University of Texas at Austin, Austin, TX, 78705, USA [b]Department of Mechanical Engineering, The University of Texas at Austin, Austin, TX, 78705, USA [c]Cardiothoracic Surgery, Spectrum Health, Grand Rapids, MI, 49503, USA [d]Department of Cardiac, Vascular, and Endovascular Surgery and Transplantology, Medical University of Silesia School of Medicine in Katowice, Silesian Centre for Heart Diseases, Zabrze, Poland [e]Department of Cardiac Surgery, Medical University of Silesia School of Medicine in Katowice, Katowice, Poland [f]Department of Biomedical Engineering, Vanderbilt University, Nashville, TN, 37235, USA [g]Department of Aerospace Engineering and Engineering Mechanics, The University of Texas at Austin, Austin, TX, 78705, USA

Abstract

The tricuspid valve ensures unidirectional blood flow from the right atrium to the right ventricle. The three tricuspid leaflets operate within a dynamic stress environment of shear, bending, tensile, and compressive forces, which is cyclically repeated nearly two billion times in a lifetime. Ostensibly, the microstructural and mechanical properties of the tricuspid leaflets have mechanobiologically evolved to optimally support their function under those forces. Yet, how the tricuspid leaflet microstructure determines its mechanical properties and whether this relationship differs between the three leaflets is unknown. Here we perform a microstructural and mechanical analysis in matched ovine tricuspid leaflet samples. We found that the microstructure and mechanical properties vary among the three tricuspid leaflets in sheep. Specifically, we found that tricuspid leaflet composition, collagen orientation, and valve cell nuclear morphology are spatially heterogeneous and vary across leaflet type. Furthermore, under biaxial tension the leaflets' mechanical behaviors exhibited unequal degrees of mechanical anisotropy. Most importantly, we found that the septal leaflet was stiffer in the radial direction and not the circumferential direction as with the other two leaflets. The differences we observed in leaflet microstructure coincide with the varying biaxial mechanics among leaflets. Our results demonstrate the structure-function

*Corresponding author: manuel.rausch@utexas.edu (Manuel K Rausch).

Disclosures

Dr. Rausch has a speaking agreement with Edwards Lifesciences. None of the other authors have any potential conflicts of interest.

Declaration of Competing Interests

The authors declare that they have no known competing financial interests or personal relationships that could have appeared to influence the work reported in this paper.

relationship for each leaflet in the tricuspid valve. We anticipate our results to be vital toward developing more accurate, leaflet-specific tricuspid valve computational models. Furthermore, our results may be clinically important, informing differential surgical treatments of the tricuspid valve leaflets. Finally, the identified structure-function relationships may provide insight into the homeostatic and remodeling potential of valvular cells in altered mechanical environments, such as in diseased or repaired tricuspid valves.

Graphical Abstract

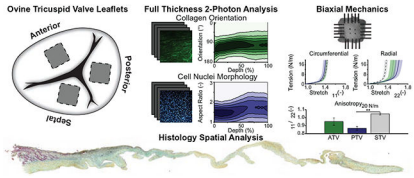

Keywords

biaxial; mechanobiology; growth and remodeling; second harmonic generation; collagen; morphology; nuclei

1. Introduction

The tricuspid valve separates the right atrium from the right ventricle of the heart. It is circumscribed by a partially fibrous annulus and comprised of three leaflets (i.e., anterior, posterior, and septal), while chordae tendineae secure each leaflet to the right ventricular myocardium. The tricuspid valve functions as one of four check valves that ensure unidirectional blood flow through the heart[1]. During diastole, the three leaflets open toward the right ventricle allowing for ventricular filling. During systole, the three leaflets coapt to prevent regurgitant blood flow into the atrium. Thus, the tricuspid valve leaflets operate cyclically within a highly dynamic environment. Specifically, in a single heart beat each tricuspid valve leaflet is exposed to shear forces from blood flow, biaxial forces from transvalvular blood pressure, tethering forces from chordae tendineae, and forces from the dilating and contracting tricuspid annulus [2, 3]. During the average human lifetime, this cycle is repeated approximately two billion times.

The compositional, microstructural, and mechanical properties of the leaflets have evolved to support the function of the tricuspid valve and resist those forces. Such changes are ostensibly driven by mechanobiological activation of valvular interstitial cells and by valvular endothelial cells undergoing endothelial-to-mesenchymal transition due to mechanical stress [4, 5]. Therefore, developing such understanding requires the relating of microstructural properties not only with mechanical properties, but also with the biologically active mediators of these changes - the native valvular cells. Understanding the structure-function relationships of the tricuspid valve leaflets is important not only from a basic scientific perspective, but also a clinical perspective. For example, surgical 25 manipulation of the leaflets during tricuspid valve repair likely changes the mechanical environment of the leaflets. Surgery may thus disturb the mechanobiological homeostasis of the resident

valvular cells and consequently of the valve tissue. As in the mitral valve, changes in mechanobiological homeostasis may ultimately result in (mal-) adaptation of the leaflets in the form of leaflet growth and remodeling [6, 7, 8, 9, 10]. Such changes may, at least in part, be responsible for the currently poor clinical outcomes of tricuspid valve surgery, i.e., approximately 35% of tricuspid valve repairs fail within the first five years after surgery [11].

Because of the erroneous notion that the tricuspid valve was the “lesser” of the two atrioventricular heart valves, its study had been lacking behind that of the mitral valve [12, 13]. Fortunately, this gap is starting to fill recently (see references [14, 15] for detailed reviews). However, there remains a need to further understand how the microstructure of tricuspid valve leaflets determines their mechanical properties. Furthermore, it is of interest whether this relationship differs between the three tricuspid valve leaflets. The distinction of inter-leaflet differences may be vital to informing differential surgical treatments of the leaflets, or more accurately informing the material properties of computational models of the tricuspid valve [16, 17, 18, 19]. Finally, as leaflet regions fulfill different functions and undergo different loading modes (i.e., the free edge is engaged in coaptation and is thus compressed during systole, while the belly is primarily biaxially stretched), analyses of spatial variations in microstructural properties may support recent spatially heterogeneous mechanical analyses of the leaflets [20].

Sheep have become one of the most widely accepted large animal models of heart disease[21]. This is particularly true for right ventricular and tricuspid valve disease [22, 23, 24, 25]. For instance, we have developed an acute and chronic model of right heart disease that presents with significant tricuspid valve regurgitation [26, 22]. One of our interests lies in quantifying the effects of chronic disease on changes in the structure-function relationship of the tricuspid valve leaflet as potential targets for therapeutic treatment. Naturally, understanding this complex relationship begins with studying the normal tricuspid valve. Therefore, the purpose of this study was to quantify and relate microstructural and mechanical properties in matched healthy ovine tricuspid valve leaflets and include an analysis of resident valve interstitial cell nuclear morphology.

2. Methods

We performed all surgical and experimental procedures according to the Principles of Laboratory Animal Care, formulated by the National Society for Medical Research, and the Guide for Care and Use of Laboratory Animals prepared by the National Academy of Science and published by the National Institutes of Health. This protocol was also approved by the local Institutional Animal Care and Use Committee (Spectrum Health IACUC No.: 18-01).

2.1. Animal Model Procedures

The tricuspid valve leaflets used in the current study were excised from sheep that were included in a previous study [27]. Detailed descriptions of the surgical procedure and medications that were used in this study are also available in our earlier work [28]. In short, healthy Dorset sheep were anesthetized, intubated, and placed on cardiopulmonary bypass.

Under bypass, but on the beating heart, we implanted sonomicrometry crystals on the tricuspid valve complex and right ventricle myocardium. After weaning the animals off cardiopulmonary bypass we waited until all hemodynamic metrics stabilized. Once we collected all marker data, we euthanized the animals, removed all sonomicrometry crystals, and excised the tricuspid valve complex tissue for inclusion in this current study.

2.2. Tissue Storage

Upon tissue excision, we photographed the unfolded tricuspid valve complexes while they floated on 1xPBS. We then isolated each leaflet at the commissures and cryogenically stored them at −80 °C in a 9:1 DMEM and DMSO solution with protease inhibitor using a controlled freezing device (*Mr. Frosty, Thermo Scientific, Waltham, MA, USA*). All leaflets remained in storage at −80 °C until testing. Before testing, we rapidly thawed the tissue in 25 °C 1xPBS and confirmed that no morphometric changes had occurred following cryogenic storage by photographing the thawed isolated leaflets in similar floating conditions as before (data not shown). We also used these photographs to characterize morphological and chordae tendineae insertion metrics from atrialis and ventricularis views of the leaflets, see Appendix A.

2.3. Histology

Upon tissue thawing, we excised a radial strip of tissue from annulus to free edge immediately adjacent to the central belly region where excised biaxial samples would later be taken for each leaflet, see Section 2.4 and Supplementary Figure S1. We fixed each radial strip in 10% neutral buffered formalin for 24 hours and then stored them in 70% ethanol. We shipped three tissue samples of each leaflet to a commercial histology service (*Histoserv, Inc., Germantown, MD, USA*) which embedded, transversely sectioned (5 μm thick), and Movat Pentachrome stained the samples. Using a light microscope (*BX53 Upright Microscope, Olympus, Tokyo, Japan*), we subsequently stitched 4X magnification images to view full radial strips. We used a custom *MATLAB* program to analyze these stitched images for regional thicknesses, see Appendix B. Additionally, we imaged representative annulus, belly, and free edge regions, defined as equally split thirds of the radial strips, with a 10X objective for constituent analysis. On these images, a custom *MATLAB* program quantified the regionally-dependent relative area fraction of structural constituents (i.e., collagen, elastin, glycosaminoglycans (GAGs), muscle/cytoplasm, fibrin) in each leaflet. Note, we verified that this analysis was not dependent on the magnification under which the images were taken, please see Supplementary Figure S2. To better visualize constituents, please refer to Supplementary Figure S3 for a sample 10X magnification image with representative constituents. At this magnification, collagen, elastin, GAGs, cell nuclei, and muscle (not pictured) are visible.

2.4. Planar Biaxial Testing

We also excised a 7 mm x 7 mm sample from the central belly region of each leaflet to be tested under planar biaxial tension and subsequent two-photon microscopy. When excising the samples, we ensured the square edges were aligned with the radial and circumferential directions of the leaflet. We first measured and averaged sample thickness from four locations using a digital thickness gauge. For (pre-)strain analyses, we marked an

approximate 3 mm x 3 mm square in the tissue center with ink dots. We then photographed these fiducial markers under floating conditions on a calibrated grid to establish a stress-free reference configuration. Next, we mounted each sample on a commercial biaxial tension testing device (*Biotester, Cellscale, Waterloo, ON, Canada*), aligning the radial and circumferential directions of the sample with the rakes of the device. Before testing, we preconditioned the samples equibiaxially to 300 mN for 10 cycles. Prior to each subsequent testing protocol, we applied a 10 mN preload to remove any tissue slack. We then performed two cycles of five different loading protocols, including equibiaxial and off-biaxial configurations (i.e., 300 mN : 300 mN, 225 mN : 300 mN, 300 mN : 225 mN, 150 mN : 300mN, 300mN : 150mN). For the final recovery stroke of each loading protocol, we recorded (5 Hz) rake-to-rake distances, forces in the radial and circumferential directions, and images of the fiducial markers to compute local tissue stretch. We performed all biaxial tests in 37 °C 1xPBS within four hours of thawing. Immediately after biaxial tension testing, we prepared the belly samples for two-photon microscopy.

2.5. Two-Photon Microscopy

On the same samples we used for mechanical testing (i.e., post mechanical testing), we applied a cell-permeant nuclear counterstain (*Hoechst 33342, Thermo Fischer Scientific, Waltham, MA, USA*) in staining buffer for 20 minutes. To ensure full thickness image acquisition, we then optically cleared the tissue in a 50:30:20% isotonic solution of Glycerol, DMSO and 5xPBS for 30 minutes under sonication. We transferred the belly samples to a two-photon microscope (*Ultima IV, Bruker, Billerica, MA, USA*) for the in vitro collagen fiber orientation analysis via second-harmonic generation (SHG) and cell nuclei morphology analysis via fluorescent excitation. During imaging, the samples were covered by coverslip and stress-free in that no external tension was applied to the tissue. We acquired all images with the atrialis surface facing the 20X water immersion objective (*XLUMPLFLN, Olympus, Center Valley, PA*). At excitation wavelengths of 900 nm and 800 nm for SHG and fluorescence, respectively, we epi-collected the backscattered signal through a PMT channel filter (460nm ± 25 nm). We imaged 500x500 μm z-stacks at three locations in the center of the sample with step sizes of 10 μm, see Supplementary Figure S1. Thus, we did not image the entire tissue but sampled the tissue at only three points which we subsequently averaged. All tissues were imaged on a foil-lined glass slide, to provide visual indication of full-thickness acquisition. After imaging, we returned the samples to 1X PBS for one hour to reverse the effect of glycerol clearing. We then prepared the samples for histology to validate unaltered tissue histology from optical clearing processes (data not shown).

To analyze the collagen fiber orientation distribution of the images, we used *ImageJ* [29]. In analyzing each image, we first normalized the image histogram based on saturation, and then passed this processed image into the *ImageJ* plugin *OrientationJ* [30]. From *OrientationJ*, we acquired a coherency-weighted histogram of fiber orientations. Using data averaging and interpolation, we represent the data from all three locations of a sample into a single z-stack of histograms by depth, where 0% and 100% depths represent the atrialis and ventricularis surfaces, respectively. We then averaged these distributions by leaflet type, acquiring an average distribution of each leaflet by depth. We then fit a von Mises

distribution to the histogram of each leaflet at each depth, which is characterized by the parameters μ and κ, i.e., the mean fiber angle and the fiber orientation concentration, respectively. We also implemented a custom *MATLAB* program which identifies each individual nucleus contour and quantifies metrics of circularity, nuclear aspect ratio (NAR), and orientation. Please see Supplementary Figure S4 for a comparison between the automatic algorithm and manual measurements of these metrics. To analyze these parameters, we implemented similar location and sample averaging and interpolation of histograms as described above. In these analyses, we fit von Mises distributions to orientation histograms and normal distributions, with parameters μ and σ (i.e. mean and standard deviation, respectively), to circularity and NAR histograms.

2.6. Biaxial Membrane Tension and Stretch Calculations

To acquire the in-plane stretch during testing, we calculated the deformation gradient tensor, **F**, with respect to the floating stress-free reference configuration via the previously acquired images of the four fiducial markers. Specifically, using linear shape functions, we computed the deformation field $\boldsymbol{\phi}$, mapping the positions of the four fiducial markers between reference and deformed configurations. The deformation gradient tensor is the material gradient of the linear deformation field, i.e., $\mathbf{F} = \nabla_{\mathbf{x}}\boldsymbol{\phi}$. We then calculated the right Cauchy-Green deformation tensor, **C**, via $\mathbf{C} = \mathbf{F}^{\mathrm{T}}\mathbf{F}$. To calculate stress, we transformed measured load data into Cauchy stress σ. To this end, we determined the deformed cross-sectional area from the deformed rake-to-rake distance and the projected deformed configuration thickness t under the assumption of tissue incompressibility. We calculated the membrane tension, **T**, as $\mathbf{T} = t\sigma$.

2.7. Statistical Analysis

For all biaxial, histological, and morphological data comparisons, we used a linear mixed effects model as implemented in *R* via the package *afex*. For all two-photon distribution data comparisons we used a linear model, as implemented in *R*. When applicable, our models included within-effects of region and depth, between-effects of leaflet type, and the interactions of those effects. Additionally, our linear mixed effects models included random effects from subject and crossed random effects between subject and within-effects. After ANOVA analyses between models, we performed appropriate multicomparison Tukey post-hoc analyses in *R* via the library *emmeans*. For all correlative analyses, we performed Pearson correlation tests. We defined statistical significance as p-values smaller than 0.05. We reported all data as mean ± standard error, unless indicated otherwise.

3. Results

3.1. Tricuspid leaflets exhibit varying degrees of mechanical anisotropy

The biaxial behavior of tricuspid valve leaflets has previously been reported, though primarily in the context of either informing mechanical constitutive models or comparing tricuspid valve leaflets to other valve leaflets [31, 32, 33, 34]. Toward providing microstructural and mechanical data in matched samples, we excised samples from the belly region of each tricuspid valve leaflet, and tested each sample under biaxial tension in radial and circumferential directions (Figure 1A). All samples exhibited the classic J-shaped

constitutive behavior of fibrous soft tissues. Under equibiaxial test conditions, the circumferential behavior of the anterior, posterior, and septal leaflets was highly consistent. The radial behavior data, however, suggested varying degrees of leaflet-dependent mechanical anisotropy (Figure 1B). In order to further investigate these differences, we quantified four metrics: toe region stiffness, stiffness at 20 N/m, transition stretch (i.e., the heel stretch of the J-shaped curve, where collagen engages), and a mechanical anisotropy index (i.e., the ratio of circumferential and radial stretches at 20 N/m) (Figure 1C). Our analysis did not reveal any significant differences among toe region stiffnesses, nor stiffnesses at 20 N/m. We observed significant differences between radial and circumferential transition stretches in the posterior leaflet ($p < 0.01$) and nearly in the anterior leaflet ($p = 0.087$), suggesting directional-dependent stretches required for collagen engagement. Additionally, we observed the radial transition stretch of the posterior leaflet to be significantly larger than that of the septal leaflet ($p < 0.05$). Strikingly, our mechanical anisotropy index analysis revealed an index greater than one for the septal leaflet indicating larger stretches in the circumferential direction than in the radial direction under equibiaxial tension. The mechanical anisotropy index of anterior and posterior leaflets was less than one indicating larger stretches in the radial direction than in the circumferential direction under equibiaxial tension. Statistical analysis revealed that leaflet type has a significant effect on leaflet mechanical anisotropy ($p < 0.01$). From post-hoc multicomparisons, we found significantly different mechanical anisotropy indices between septal and posterior leaflets ($p < 0.01$), while the other pairwise comparisons failed to meet significance (anterior-posterior: $p = 0.14$, anterior-septal: $p = 0.09$). Overall, our analysis identified varying degrees of leaflet mechanical anisotropy under equibiaxial tension, i.e., the septal leaflet has greater circumferential compliance, while the anterior and posterior leaflets have greater radial compliance.

3.2. Tricuspid leaflet constituents vary spatially

Previous studies have reported tricuspid valve constituent analyses [33], but there is limited data regarding their spatial variation within and between leaflets. To perform these analyses, we colorimetrically analyzed Movat's Pentachrome stained histological sections of radial strips (i.e., from annulus to free edge) immediately adjacent to previously excised biaxial samples (Figure 2A).

We quantified the area fractions of five constituents from Movat's Pentachrome staining: GAGs (blue), collagen (yellow), elastin (black), muscle/cytoplasm (purple), and fibrin (red, data not shown) (Figure 2B). For spatial analyses, we define approximations for annulus, belly, and free edge regions as equally split thirds of the radial strips. We separated our comparisons into within-leaflet and between-leaflet differences. In comparing GAG area fractions, the septal leaflet free edge GAG content was less than that in the annulus ($p < 0.05$) or belly ($p < 0.01$) regions. Additionally, in the belly region, the GAG area fraction was larger in the septal leaflet than in the anterior leaflet ($p < 0.05$). For collagen area fractions, the septal leaflet free edge collagen content was greater than that in the annulus ($p < 0.05$) or belly ($p < 0.01$) regions. Similarly, the posterior leaflet free edge collagen content was greater than that in the belly and annulus regions (both $p < 0.05$). Additionally, in the belly region, the collagen area fraction was larger in the anterior leaflet than in the septal

leaflet ($p < 0.05$). For elastin area fractions, our analysis revealed no within-leaflet or between-leaflet differences, likely due to large inter-subject variability. For muscle/cytoplasm area fractions, all significant findings involved comparisons with the annulus region, which is likely due to the peri-annular muscle integrating in annular regions of the leaflet, and not necessarily attributed to cell count, see Figure 2A, posterior. Overall, our area fraction analysis suggests that constituents are heterogeneously distributed and that there are compositional differences between leaflets.

3.3. Collagen fiber orientation and concentration varies by depth and leaflet

Collagen is the major structural protein responsible for the tensile properties of biological materials [35]. Therefore, studying collagen structure and orientation is important when relating microstructure to mechanical behavior. However, collagen structure analyses of tricuspid valve leaflets have only been reported via bulk tissue small-angle light scattering analyses [36] and single-depth SHG imaging [34], two methods which have limited z-direction spatial resolution. To fill this gap, we utilized two-photon microscopy to acquire full-thickness images of collagen via SHG in the same tricuspid valve leaflet belly samples that were mechanically tested.

In Figure 3A, representative images of collagen are shown from within the indicated depth regions, where 0% depth represents the atrialis surface, and horizontal fibers align with the circumferential direction. Although the anatomical layers are difficult to delineate from SHG images alone, we adopt three general regions, i.e., 0-33%, 33-67%, and 67-100% depths, as approximate definitions for atrialis, spongiosa, and fibrosa/ventricularis, respectively. Subsequently, we analyzed the collagen orientation throughout the leaflet depths, see Figure 3B, with 90° aligning circumferentially. We summarized the von Mises distribution parameters μ and κ for the collagen orientation distributions (i.e., mean and concentration, respectively) in the same three regions for statistical comparison. Additionally, we report the von Mises distribution parameters in Table 1 by depth and for each leaflet. Note that larger values for concentration parameter, κ, indicate more concentrated collagen fiber orientations. We found that collagen mostly aligned circumferentially throughout the leaflet thickness. However, we found statistically significant differences in the mean collagen direction of the atrialis for all three leaflets when compared to that in the spongiosa and fibrosa/ventricularis layers (all $p < 0.0001$). Specifically, we found a consistent radial shift of the collagen orientation in the atrialis of all leaflets, which was most prominent in the septal leaflet. Furthermore, we found statistically significant differences between the mean collagen direction of the septal leaflet when compared to the anterior and posterior leaflets in the spongiosa ($p < 0.01$ and $p < 0.001$, respectively) and fibrosa/ventricularis ($p < 0.05$ and $p < 0.001$, respectively) layers. Additionally, in anterior leaflets we found significantly smaller fiber orientation concentrations in the atrialis and fibrosa/ventricularis than in the spongiosa (both $p < 0.0001$). In posterior leaflets, we found no significant differences in fiber orientation concentrations between layers. In septal leaflets, we found significantly lower orientation concentrations in the fibrosa/ventricularis than in the atrialis and spongiosa layers (both $p < 0.0001$). Across leaflets, we found that the septal leaflet showed significantly lower fiber orientation concentration in the fibrosa than the anterior and posterior leaflets (both $p < 0.0001$). Additionally, the posterior leaflet showed significantly

higher fiber orientation concentration in the atrialis than in the anterior and septal leaflets (both $p < 0.0001$).

In our analysis, we also noted a qualitative change in collagen morphology at different depths. In the atrialis, collagen organized as individual fibers, typically shifting from fibers with radial and circumferential components toward mostly circumferential fibers. In the spongiosa, collagen was still organized as individual fibers but was mostly aligned circumferentially. In the fibrosa/ventricularis, collagen organized into what appears to be higher-order sheets aligned circumferentially, most notably in posterior leaflets.

Overall, our SHG data suggest that collagen is aligned primarily in the circumferential direction throughout all leaflet depths. Some radial direction variability arises from mean direction shifts in the atrialis (posterior and septal leaflets), or low fiber orientation concentration in the atrialis (anterior and septal) and fibrosa/ventricularis (septal). Additionally, collagen qualitatively appeared as individual fibers in the atrialis and spongiosa for all leaflets, but was organized sheets in the fibrosa/ventricularis, especially in posterior leaflets.

3.4. Cell nuclei morphology agrees with collagen organization

Resident valve cells and their nuclei are mechanobiologically active constituents responsible for maintaining the valvular extracellular matrix. Valvular interstitial cells and their response to mechanical stimuli have been investigated in the aortic and mitral valves [37, 38]. However, tricuspid valvular interstitial cells have not received this same attention. Toward an initial understanding, we utilized two-photon microscopy to perform full-thickness image acquisition of cell nuclei via *Hoechst 33342* fluorescence. We captured these images in the same tricuspid valve leaflet belly sample previously imaged for collagen SHG (Figure 4A). We report the von Mises distribution parameters of nuclei orientation and the normal distribution parameters of NAR and circularity by depth for each leaflet in Table 2. As before, we refer to 0-33%, 33-67%, and 67-100% regions as atrialis, spongiosa, and fibrosa/ventricularis respectively. Interestingly, we found that cell nuclei orientation varied by leaflet and depth in similar ways that collagen orientation varied by leaflet and depth (Figure 4B). Pearson correlative analysis between mean collagen orientation and mean nuclei orientation through the depth of each leaflet showed strong linear correlation (Anterior: $r = 0.708$, Posterior: $r = 0.934$, Septal: $r = 0.954$, all $p < 0.0001$). Specifically, we found that nuclei mostly aligned circumferentially throughout the leaflet thickness. Similar to collagen, we found significant radial shifts in the mean nuclei direction in the atrialis of all three leaflets when compared to the spongiosa and fibrosa/ventricularis layers (Anterior: $p < 0.001$, Posterior, Septal: $p < 0.0001$). We also found the mean nuclei direction of the septal leaflet varied significantly from the anterior and posterior leaflets in the fibrosa/ventricularis layers ($p < 0.01$ and $p < 0.05$, respectively). Additionally, we found lower nuclei orientation concentration in the atrialis of all three leaflets (all $p < 0.0001$), possibly due to the more circular shapes of the nuclei in this layer. Furthermore, we found that the septal leaflet nuclei orientations were less concentrated in the fibrosa/ventricularis than in the anterior and posterior leaflets (both $p < 0.0001$). Overall, our data suggest that cell nuclei orientation agrees with the respective leaflet's collagen orientation pattern.

Qualitatively, we observed cell nuclei morphology to vary by depth (Figure 4A). Quantitatively, we measured the NAR and circularity of each nucleus to quantify the elliptical and irregular shapes, respectively, by leaflet and depth (Figure 4C,D). Specifically, across all three leaflets, we observed that atrialis nuclei were significantly more circular (i.e., NAR nearer 1) than fibrosa/ventricularis layer nuclei (all $p < 0.0001$). The NAR transitioned to more oblong shapes consistently within the spongiosa layer. Additionally, the septal leaflet nuclei in the fibrosa/ventricularis were less oblong than anterior and posterior leaflet nuclei (both $p < 0.01$). For circularity, we observed similar shape transitions in the spongiosa. In all three leaflets, atrialis nuclei were significantly more regular shaped (i.e., circularity nearer 1) than fibrosa/ventricularis layer nuclei (all $p < 0.0001$) which possessed more irregular undulated shapes. This transition in circularity consistently occurred within the spongiosa layer. Additionally, the septal leaflet nuclei shapes were significantly more regular than anterior and posterior leaflet nuclei in the fibrosa/ventricularis (both $p < 0.0001$). Overall, our findings suggest that near the spongiosa, cell nuclei shifted from circular to irregular elliptical shapes, most drastically in anterior and posterior leaflets.

4. Discussion

The tricuspid valve has historically received less attention than the aortic and mitral valves, each of which are associated with left heart disease [12, 13]. As research is focusing on right heart disease, tricuspid valve disease is becoming recognized as a significant source of morbidity and mortality [39, 40, 41]. Toward a greater understanding of tricuspid valve disease, a critical component to discern is the relationship between tissue microstructure and leaflet mechanics, first in health, and ultimately in disease. In our current work, we performed a matched investigation of biaxial mechanical behavior with a full-thickness analysis of microstructural properties and native cell nuclei morphology in healthy ovine tricuspid valve leaflets. The novelty of our work lies, among other results, in: i) This being the first report on the leaflet-specific, biaxial mechanical behavior and morphology of ovine tricuspid valve leaflets, ii) this being the first report on the leaflet-specific, depth-resolved microstructure and cell shape/orientation in tricuspid valve leaflets, and iii) this being the first report on the leaflet-specific, correlation between the depth-dependent microstructural orientation and cell orientation in tricuspid valve leaflets.

In our study, the tricuspid valve leaflets showed a distinct J-shaped constitutive behavior under biaxial tension. This finding is consistent with our understanding of the behavior of collageneous soft tissues [35] and has been reported by numerous investigators [31, 34, 20] and in various species [32, 33, 42]. We added to the current body of literature by carefully referencing our mechanical data to a “floating” stress-free reference configuration, rather than a pre-stretched state. Our choice of this reference configuration was inspired by a previous study on murine skin where we found that even small pre-loads (in the mN range) during biaxial testing can significantly alter the interpretation of biaxial data [43]. This sensitivity follows from the highly compliant behavior of these tissues at small forces. The discrepancy in reference configurations between our current study and previous studies may explain incongruencies in the observed behaviors. Specifically, we observed that leaflets were more compliant than reported elsewhere [31, 20, 34]. Additionally, we observed a smaller degree of mechanical anisotropy (i.e., ratios closer to 1, or near isotropic) when

compared to some previous reports [34, 32, 33]. These discrepancies may also be due to species differences or testing protocol differences.

Additionally, we added to previous reports by including all three leaflets in our mechanical analysis. Thereby, we revealed that all three leaflets show a nearly identical behavior in the circumferential direction, while showing differing behavior in the radial direction. The anterior and posterior leaflets stretched less in the circumferential direction than in the radial direction. In contrast, the septal leaflet stretched less in the radial direction than in the circumferential direction. We are the first to have noted this difference in mechanical anisotropy. It may be speculated that the septal leaflet's unique behavior among the tricuspid leaflets follows from its reduced range of motion when compared to the other two leaflets. Specifically, we recently reported on the in vivo strains of the ovine tricuspid valve leaflets [27]. There we found that the septal leaflet has a smaller opening angle (30° vs. 60° (anterior) and 45° (posterior)). Additionally, the septal leaflet took a convex shape during systole as opposed to the other two leaflets that were predominantly concave. Furthermore, previous studies have shown that the septal region of the tricuspid annulus is the most fibrous and stiffest [44, 45, 46], which may explain the altered motion of the septal leaflet. These differences in septal leaflet motion and dynamic shape may create a mechanical state that favors increased matrix deposition in the radial direction (see also discussion on collagen organization below).

Naturally, the mechanical behavior of soft collagenous tissues is determined by its constituents and their microstructural organization. While the tricuspid leaflet composition has previously been analyzed and reported, we added an area fraction-based, spatially-resolved analysis. Of particular interest were collagen, elastin, and GAGs. Elastin is thought to determine the mechanical behavior of soft collagenous tissues at small stretches, when the undulated collagen fibers are not yet activated [47]. In contrast, collagen is thought to provide strength at higher stretches as the fibers progressively recruit and uncrimp [35]. On the other hand, GAGs are thought to lubricate and support regions of tissue that undergo shear and compression, attributed to their ability to sequester (income-pressible) water [48, 49]. Thus, GAGs have been proposed to support leaflet function at the free edge, where hydrostatic forces on the ventricularis side and contact from opposing leaflets on the atrialis side create compressive environments [49]. We did not find significant differences in elastin content between leaflets or within leaflets. On the other hand, we did find that collagen and GAGs varied by location and leaflet. Interestingly, GAGs were least abundant in the free edge, contradicting the above hypothesis. Surprisingly, there was evidence that collagen was more abundant in the free edge than elsewhere. This finding is particularly interesting and may suggest that leaflet stretch, rather than compression, occurs at the free edge, possibly due to chordal attachment at the free edge. Finally, collagen appeared more abundantly in the anterior leaflet than in the other leaflets. This point is particularly interesting in light of our recent observation that the anterior leaflet undergoes the largest in vivo strains. This may suggest that increased stress increases mechanobiologically-mediated matrix deposition.

In our analysis, we quantified collagen orientation in the leaflets' bellies throughout their thickness. Being the principal structural protein, collagen orientation is thought to determine the tissue's axes of mechanical anisotropy [35]. We found that collagen was predominantly

oriented in the circumferential direction throughout the thickness of the leaflets, with a small radial shift in the atrialis of all leaflets. This radial shift is likely due to the atrialis' surface exposure to radial shear stress from blood flow in vivo. Overall, the orientation of collagen does indeed coincide with the principal axis of mechanical anisotropy, except for septal leaflets. As mentioned above, the septal leaflet appeared to stretch less in the radial direction than in the circumferential direction. Thus, there seems to be an inconsistency between the preferred mechanical direction of anisotropy and the mean fiber direction of collagen. This inconsistency may be, at least in part, explained by the low collagen fiber orientation concentration in the septal leaflet, its smaller degree of organization in the normally collagen-dense fibrosa, and the relatively low overall collagen density. The latter point may imply that other structural components may have a larger weight in determining the septal leaflet mechanics than in the other two leaflets. Additionally, we consider the effect of surrounding components - its annulus and chordae tendineae - on a potentially unique stress environment for the septal leaflet, resulting in a unique collagen microstructure. As mentioned before, the septal region of the tricuspid valve annulus is uniquely more fibrous and stiffer than the rest of its perimeter [44, 45, 46]. Consistently, we have also noted a reduced dynamic range within the septal region of the human and ovine annulus throughout the cardiac cycle [50, 51]. Therefore, we hypothesize the fibrous septal annulus may effectively shield the septal leaflet from large circumferential strains in vivo. This point can be further corroborated by our recent finding that ovine septal leaflet belly regions undergo the smallest in vivo circumferential strains among leaflets[27]. We also observed that the septal leaflet possessed unique chordal attachments. Specifically, septal leaflet chordae attached closer to the leaflet midline and inserted at radial angles more often than other leaflets' chordae, see Appendix A, (Figure A1G–J). As chordae tendineae are organized unidirectional collagen structures and attach to the collagen-rich fibrosa/ventricularis, their insertion angle likely influences surrounding collagen orientation and the direction of applied stresses. Thus, the septal leaflet, with the most radially oriented chordae tendineae insertion angles, may experience more radial stresses, increasing the likelihood of radial collagen deposition. Overall, we hypothesize that the unique mechanical behavior of the septal leaflet may be, in part, attributed to annular stress shielding and radial tethering, creating a stress environment more favorable for circumferential collagen degradation and radial collagen deposition.

It has been shown in other valvular leaflets that mechanical stimuli can activate valvular interstitial cells rendering them myofibroblast-like [52, 53, 54] and result in transdifferentiation of vascular endothelial cells into a synthetic phenotype via endothelial-to-mesenchymal transition [37, 10]. Both cell types may be involved in the maintenance and remodeling of their surrounding extracellular matrix [55, 4, 56]. We found that cell nuclei consistently aligned with their surrounding collagen in all three leaflets. Additionally, the cell NAR and nuclei circularity consistently shifted from round to more elliptical and irregular shapes between the atrialis and fibrosa/ventricularis layers of the leaflets. This trend occurred most drastically in anterior and posterior leaflets. We speculate that the highly organized collagen sheets we observed in these leaflets may impose spatial limitations onto the cells and their nuclei and thereby influence the morphology of the nuclei. When considered together, morphological metrics of cell nuclei shape may be

reflective of stress environments in different layers. It may be speculated, for example, that cell nuclei in the atrialis are rounded as they are exposed to low oscillatory shear from adjacent blood flow. Conversely, cell nuclei may be elongated in the fibrosa/ventricularis due to exposure to high biaxial tension and shear. Cell nuclei orientation may also identify deformational susceptibilities during abnormal stress environments, such as in disease, that can result in transdifferentiation and increased extracellular matrix remodeling. Altogether, these spatially-resolved morphological metrics of cell nuclei may provide additional knowledge about the homeostatic and remodeling potential of the mechanobiologically sensitive valvular cells within leaflets.

Our leaflet-dependent analyses may become critically important as they provide insight into how surgical/interventional repair could differentially affect the mechanobiologically sensitive valve leaflets. This is particularly important to novel, transcatheter approaches such as the TriClip or PASCAL devices [57]. These devices hold the key to treating the large population of patients with tricuspid regurgitation that are currently not being treated [58]. For example, the TriClip device, which mimics edge-to-edge repair, is applied to approximate/fuse any two leaflets. Understanding the leaflet-specific mechanical and biological properties could inform the decision which leaflets to clip to minimize the risk of short-term (e.g., tissue tearing) and long-term (e.g., fibrotic tissue remodeling) failure.

Our study is naturally subject to several limitations. Primarily, we performed this study on ovine, not human tissue. Thus, any extrapolation of our findings to humans must be done with care. Additionally, previous studies have identified the tricuspid valve as a spatially heterogeneous tissue. Multiple approaches in this study, namely histology and two-photon microscopy, simplify complex three-dimensional structures into planar observations and thus may lose valuable third-dimension information. Additionally, two-photon microscopy is a highly localized imaging technique that allows for detailed, but spatially constrained observations. Therefore our study may, in the future, be well-complemented with a bulk structural observation method, such as small angle light scattering. Furthermore, our study would be further complemented by a cell shape analysis, as mechanobiological processes in cells are not solely initiated by nuclear deformation. Lastly, the biaxial behavior of tricuspid valve leaflets has been shown to be spatially heterogeneous and our study only characterized the mechanics and microstructure of belly region samples, leaving additional analyses to be performed on samples from other leaflet regions [20]. Finally, as all mechanical tests, ours may potentially be affected by boundary effects. However, as per Saint Vernant’s principle, we analyzed strain in the sample center, away from the boundaries. While others have accounted for the boundary effects due to the rake insertions, we found that the small reported error accrued by ignoring such effects are negligible in comparison to the inter-subject variations that we observed in our study [59].

5. Conclusion

In this work, we simultaneously investigated the compositional, microstructural, and mechanical properties of the three ovine tricuspid leaflets. We found that the composition of collagen and GAGs is spatially heterogeneous within leaflets, and varies across leaflets. Also, we found that the microstructural and mechanical properties vary among the three

tricuspid leaflets and that variations in microstructural properties between leaflets correlate with varying mechanical properties. Specifically, collagen (and cell nuclei) orientation align mostly circumferentially, with varying radial deviations among leaflets in the atrialis and fibrosa/ventricularis regions. Correspondingly, the anterior and posterior leaflets demonstrated higher stiffness in the circumferential direction. Interestingly, we found that the septal leaflet (in contrast to the other two leaflets) was stiffer in the radial direction than in the circumferential direction. We anticipate that our results will be vital toward developing more accurate, leaflet-specific tricuspid valve computational models and could be used toward tissue engineering heart valve replacements. Additionally, our findings may provide clinical insight into how surgical repair could differentially affect the mechanobiologically sensitive valve leaflets, and thus inform leaflet-specific surgical treatments.

Supplementary Material

Refer to Web version on PubMed Central for supplementary material.

Acknowledgements

The authors would like to thank the University of Texas at Austin Department of Statistics and Data Science for their consultation. Research reported in this publication was supported by the National Heart, Lung, And Blood Institute of the National Institutes of Health under Award Number F31HL145976 and the American Heart Association for their support under Award Number 18CDA34120028. The content is solely the responsibility of the authors and does not necessarily represent the official views of the National Institutes of Health or the American Heart Association.

Appendix A.

Tricuspid valve morphology and chordal insertions vary by leaflet

Previous reports have described the different sizes and shapes of the tricuspid valve leaflets [60], but limited quantification of their morphological metrics exist for ovine tissue. Therefore, we quantified leaflet area, perimeter, major cusp height, and major cusp width from images of isolated leaflets (Figure A1A–B). Total leaflet perimeter was largest for posterior leaflets (107 ± 5 mm) when compared to anterior (78 ± 2 mm, $p < 0.001$) and septal leaflets (79 ± 3 mm, $p < 0.001$) (Figure A1C). Additionally, posterior leaflets had a larger total area (362 ± 28 mm^2) than septal leaflets (258 ± 14mm^2, $p < 0.01$). Anterior leaflet area (314 ± 23 mm^2) was not found to be significantly different from posterior ($p = 0.21$) and septal ($p = 0.13$) leaflets (Figure A1D). Major cusp height was largest in anterior leaflets (19.1 ± 0.8 mm) when compared to posterior and septal leaflets (16.1 ± 0.4 mm, 15.4 ± 0.4 mm, respectively, both $p < 0.01$) (Figure A1E). No significant differences were found between the major cusp width of anterior, posterior, or septal leaflets (19 ± 1 mm, 21 ± 2 mm, 23 ± 2 mm, respectively) (Figure A1F). Overall, our studies suggest that the posterior leaflet has the largest perimeter and a larger area than the septal leaflet, while the anterior leaflet has the largest major cusp height.

Additionally, we analyzed chordal insertion sites for each leaflet using images of floating isolated leaflets from the ventricularis side (Figure A1H). Specifically, we quantified the chordal insertion site distance from the major cusp radial midline, as well as the chordal

insertion angle relative to the midline, see Figure A1I–J. Interestingly, we found the septal leaflet chordal insertion sites to be closest to the radial midline (Anterior, $p < 0.001$ and Posterior, $p = 0.012$). Furthermore, the chordae tendineae of septal leaflets attached at angles aligned with the radial direction of the cusp (i.e., the radial midline) more often than in anterior and posterior leaflets (both $p < 0.0001$). Combined, these data may explain the unique radial mechanical behavior and microstructure of septal leaflets we observed. More explicitly, chordae tendineae are highly organized unidirectional collagenous structures, see Figure A1G. These chordae integrate directly into the collagen-rich fibrosa/ventricularis and likely influence the immediate collagen within the leaflet. As septal leaflets possessed more chordae near the midline (i.e., the location of excised biaxial test samples) with radial insertion angles, the stress environment they create on the septal leaflet in vivo may be unique from the other leaflets, and thus influence radial collagen deposition.

Appendix B.

Tricuspid leaflet thicknesses vary spatially

We measured the leaflet thicknesses by radial position (Figure B1A) and distributed these data into three bins: 0-33%, 33-67%, and 67-100% of their normalized radial length, generally representing the annulus, belly, and free edge regions, respectively (Figure B1B). We separated our comparisons as within-leaflet differences (e.g. anterior annulus vs. anterior belly, etc.) and between-leaflet differences (e.g. anterior belly vs. posterior belly, etc.). For within-leaflet differences, the posterior leaflet was significantly thicker in the annular region (445 ± 49 μm) compared to the belly and free edge regions (259 ± 33 μm, and 273 ± 59 μm, respectively, $p < 0.05$). The septal leaflet was significantly thicker in the annular region (350 ± 44 μm) than in the free edge region (160 ± 43 μm, $p < 0.05$). The anterior leaflet did not reveal any significant regional thickness differences. For between-leaflet differences, the anterior belly region is the thickest (429 ± 21 μm) compared to posterior and septal belly thicknesses (259 ± 33 μm, and 272 ± 33 μm, respectively, $p < 0.05$). The anterior and posterior free edge thicknesses (326 ± 20 μm, and 274 ± 59 μm, respectively) were both thicker than the septal free edge (160 ± 43 μm, $p < 0.01$ and $p < 0.05$, respectively). Overall, our analyses suggest that the posterior and septal leaflet thicknesses vary by radial position, the anterior leaflet had the thickest belly region, and the septal leaflet had the thinnest free edge region.

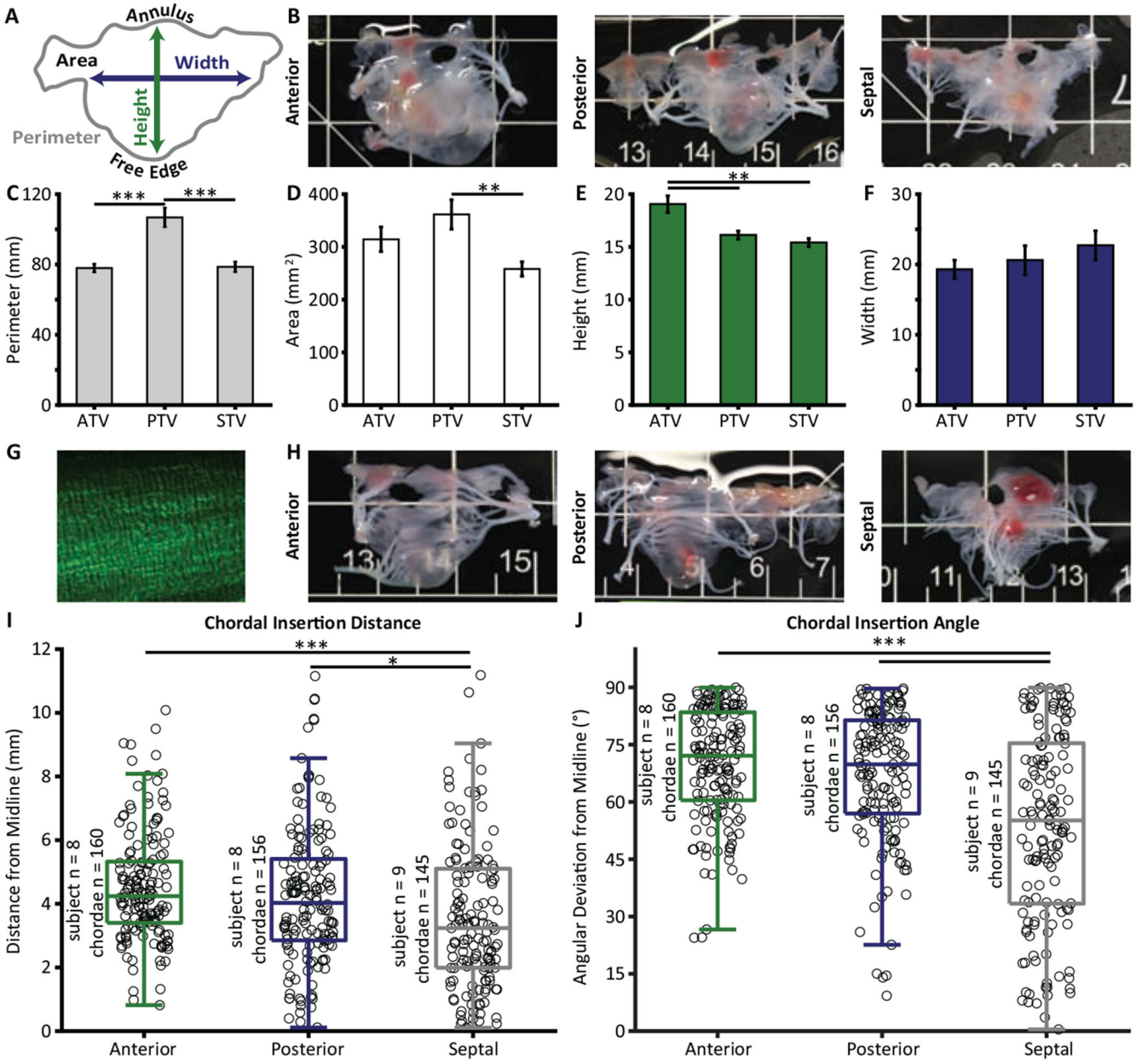

Figure A1:

Tricuspid valve leaflet morphology and chordal insertions vary among leaflets. (A) Definitions of leaflet perimeter, area, major cusp height, and major cusp width. (B) Representative images of atrialis view of anterior, posterior, and septal leaflets (grid = 12.7 mm x 12.7 mm). White asterisks denote biopsy punch taken for a separate study. (C-F) Quantification of (C) perimeter, (D) area, (E) major cusp height, and (F) major cusp width, denoted as mean ± SEM (n = 6 per leaflet). (G) Representative two-photon image of collagen showing unidirectional collagen in direction of chordal length (white arrow), scale bar = 100μm, (H) Representative images of ventricularis view of anterior, posterior, and septal leaflets (grid = 12.7 mm x 12.7 mm). White asterisks denote biopsy punch taken for a separate study. (I-J) Jitter plots denoting (I) chordal insertion distances measured from major

cusp radial midline, and (J) chordal insertion angles measured as the deviation from the major cusp radial midline. Number of chordae sampled is denoted in jitter plot ($n = 8$ anterior and posterior leaflets, $n = 9$ septal leaflets, $*p < 0.05$, $**p < 0.01$, $***p < 0.001$)

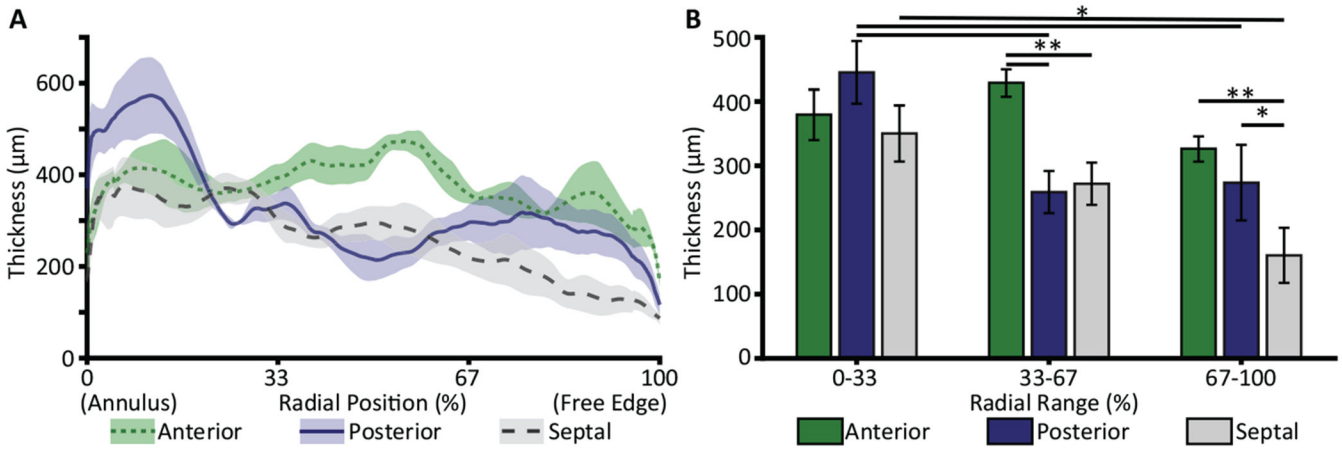

Figure B1:

(A) Leaflet thickness based on histology images varies by normalized radial position and is (B) summarized in radial bins. All data presented as mean ± SEM. ($n = 3$ per leaflet, *$p < 0.05$, * * $p < 0.01$)

References

[1]. Silver MD, Lam JHC, Ranganathan N, Wigle ED, Morphology of the human tricuspid valve, Circulation 43 (3) (1971) 333–348. [PubMed: 5544987]

[2]. Sacks MS, Yoganathan AP, Heart valve function: A biomechanical perspective, Philosophical Transactions of the Royal Society B: Biological Sciences 362 (1484) (2007) 1369–1391.

[3]. Rausch MK, Mathur M, Meador WD, Biomechanics of the tricuspid annulus: A review of the annulus' in vivo dynamics with emphasis on ovine data, GAMM-Mitteilungen (2019) e201900012.

[4]. Levine RA, Hagége AA, Judge DP, Padala M, Dal-Bianco JP, Aikawa E, Beaudoin J, Bischoff J, Bouatia-Naji N, Bruneval P, Butcher JT, Carpentier A, Chaput M, Chester AH, Clusel C, Delling FN, Dietz HC, Dina C, Durst R, Fernandez-Friera L, Handschumacher MD, Jensen MO, Jeunemaitre XP, Marec HL, Tourneau TL, Markwald RR, Merot J, Messas E, Milan DP, Neri T, Norris RA, Peal D, Perrocheau M, Probst V, Puceat M, Rosenthal N, Solis J, Schott J-J, Schwammenthal E, Slaugenhaupt SA, Song J-K, Yacoub MH, Mitral valve diseasemorphology and mechanisms, Nature Reviews Cardiology 12 (12) (2015) 689–710. [PubMed: 26483167]

[5]. Ayoub S, Ferrari G, Gorman RC, Gorman JH, Schoen FJ, Sacks MS, Sacks MS, Heart valve biomechanics and underlying mechanobiology, Comprehensive Physiology 6 (4) (2016) 1743–1780. [PubMed: 27783858]

[6]. Beaudoin J, Dal-Bianco JP, Aikawa E, Bischoff J, Guerrero JL, Sullivan S, Bartko PE, Handschumacher MD, Kim D-H, Wylie-Sears J, Aaron J, Levine RA, Mitral leaflet changes following myocardial infarction, Circulation: Cardiovascular Imaging 10 (11).

[7]. Stephens EH, Nguyen TC, Itoh A, Ingels NB, Miller DC, Grande-Allen KJ, The effects of mitral regurgitation alone are sufficient for leaflet remodeling, Circulation 118 (14_suppl_1) (2008) S243–S249. [PubMed: 18824762]

[8]. Sielicka A, Sarin EL, Shi W, Sulejmani F, Corporan D, Kalra K, Thourani VH, Sun W, Guyton RA, Padala M, Pathological remodeling of mitral valve leaflets from unphysiologic leaflet mechanics after undersized mitral annuloplasty to repair ischemic mitral regurgitation, Journal of the American Heart Association 7 (21) (2018) e009777. [PubMed: 30571381]

[9]. Rausch MK, Tibayan FA, Craig Miller D, Kuhl E, Evidence of adaptive mitral leaflet growth, Journal of the Mechanical Behavior of Biomedical Materials 15 (2012) 208–217. [PubMed: 23159489]

[10]. Dal-Bianco JP, Aikawa E, Bischoff J, Guerrero JL, Handschumacher MD, Sullivan S, Johnson B, Titus JS, Iwamoto Y, Wylie-Sears J, Levine RA, Carpentier A, Active adaptation of the tethered mitral valve: Insights into a compensatory mechanism for functional mitral regurgitation, Circulation 120 (4)(2009) 334–342. [PubMed: 19597052]

[11]. Ejiofor JI, Neely RC, Yammine M, McGurk S, Kaneko T, Leacche M, Cohn LH, Shekar PS, Surgical outcomes of isolated tricuspid valve procedures: repair versus replacement, Annals of Cardiothoracic Surgery 6 (3) (2017) 214–222. [PubMed: 28706864]

[12]. Stephens EH, Borger MA, Forgotten valve or enigmatic valve? Further insights into the tricuspid valve in patients undergoing mitral valve surgery, The Journal of Thoracic and Cardiovascular Surgery 148 (5) (2014) 1962–1964. [PubMed: 25444187]

[13]. Mascherbauer J, Maurer G, The forgotten valve: Lessons to be learned in tricuspid regurgitation, European Heart Journal 31 (23) (2010) 2841–2843. [PubMed: 20729224]

[14]. Meador WD, Mathur M, Rausch MK, Tricuspid valve biomechanics: A brief review, Springer International Publishing, Cham, 2018, pp. 105–114.

[15]. Lee C-H, Laurence DW, Ross CJ, Kramer KE, Babu AR, Johnson EL, Hsu M-C, Aggarwal A, Mir A, Burkhart HM, Towner RA, Baumwart R, Wu Y, Mechanics of the tricuspid valveFrom clinical diagnosis/treatment, in-vivo and in-vitro investigations, to patient-specific biomechanical modeling, Bioengineering 6 (2) (2019) 47.

[16]. Singh-Gryzbon S, Sadri V, Toma M, Pierce EL, Wei ZA, Yoganathan AP, Development of a computational method for simulating tricuspid valve dynamics, Annals of Biomedical Engineering 47 (6) (2019) 1422–1434. [PubMed: 30859434]

[17]. Stevanella M, Votta E, Lemma M, Antona C, Redaelli A, Finite element modelling of the tricuspid valve: A preliminary study, Medical Engineering & Physics 32 (10) (2010) 1213–1223. [PubMed: 20869291]

[18]. Kong F, Pham T, Martin C, McKay R, Primiano C, Hashim S, Kodali S, Sun W, Finite element analysis of tricuspid valve deformation from multi-slice computed tomography images, Annals of Biomedical Engineering 46 (8) (2018) 1112–1127. [PubMed: 29663193]

[19]. Kamensky D, Xu F, Lee C-H, Yan J, Bazilevs Y, Hsu M-C, A contact formulation based on a volumetric potential: Application to isogeometric simulations of atrioventricular valves, Computer Methods in Applied Mechanics and Engineering 330 (2018) 522–546. [PubMed: 29736092]

[20]. Laurence D, Ross C, Jett S, Johns C, Echols A, Baumwart R, Towner R, Liao J, Bajona P, Wu Y, Lee C-H, An investigation of regional variations in the biaxial mechanical properties and stress relaxation behaviors of porcine atrioventricular heart valve leaflets, Journal of Biomechanics 83 (2019) 16–27. [PubMed: 30497683]

[21]. Ali ML, Kumar SP, Bjornstad K, Duran CM, The sheep as an animal model for heart valve research, Vascular 4 (4) (1996) 543–549.

[22]. Malinowski M, Proudfoot AG, Langholz D, Eberhart L, Brown M, Schubert H, Wodarek J, Timek TA, Large animal model of functional tricuspid regurgitation in pacing induced end-stage heart failure, Interactive Cardio Vascular and Thoracic Surgery 24 (6) (2017) 905–910.

[23]. Rausch MK, Malinowski M, Meador WD, Wilton P, Khaghani A, Timek TA, The effect of acute pulmonary hypertension on tricuspid annular height, strain, and curvature in sheep, Cardiovascular Engineering and Technology 9 (3) (2018) 365–376. [PubMed: 29858822]

[24]. Malinowski M, Schubert H, Wodarek J, Ferguson H, Eberhart L, Langholz D, Jazwiec T, Rausch MK, Timek TA, Tricuspid annular geometry and strain after suture annuloplasty in acute ovine right heart failure, The Annals of Thoracic Surgery 106 (6) (2018) 1804–1811. [PubMed: 29958829]

[25]. Bothe W, Kvitting J-PE, Rausch MK, Timek TA, Swanson JC, Liang DH, Walther M, Kuhl E, Ingels NB, Miller DC, Do annuloplasty rings designed to treat ischemic/functional mitral regurgitation alter left-ventricular dimensions in the acutely ischemic ovine heart?, The Journal of Thoracic and Cardiovascular Surgery.

[26]. Malinowski M, Proudfoot AG, Eberhart L, Schubert H, Wodarek J, Langholz D, Rausch MK, Timek TA, Large animal model of acute right ventricular failure with functional tricuspid regurgitation, International Journal of Cardiology 264 (2018) 124–129. [PubMed: 29776560]

[27]. Mathur M, Jazwiec T, Meador WD, Malinowski M, Goehler M, Ferguson H, Timek TA, Rausch MK, Tricuspid valve leaflet strains in the beating ovine heart, Biomechanics and Modeling in Mechanobiology (2019) 1–11.

[28]. Malinowski M, Wilton P, Khaghani A, Langholz D, Hooker V, Eberhart L, Hooker RL, Timek TA, The effect of pulmonary hypertension on ovine tricuspid annular dynamics, European Journal of Cardio-Thoracic Surgery 49 (1) (2016) 40–45. [PubMed: 25755186]

[29]. Schindelin J, Arganda-Carreras I, Frise E, Kaynig V, Longair M, Pietzsch T, Preibisch S, Rueden C, Saalfeld S, Schmid B, Tinevez J-Y, White DJ, Hartenstein V, Eliceiri K, Tomancak P, Cardona A, Fiji: An open-source platform for biological-image analysis, Nature Methods 9 (7) (2012) 676–682. [PubMed: 22743772]

[30]. Rezakhaniha R, Agianniotis A, Schrauwen JTC, Griffa A, Sage D, Bouten CVC, van de Vosse FN, Unser M, Stergiopulos N, Experimental investigation of collagen waviness and orientation in the arterial adventitia using confocal laser scanning microscopy, Biomechanics and Modeling in Mechanobiology 11 (3-4) (2012) 461–473. [PubMed: 21744269]

[31]. Amini Khoiy K, Amini R, On the biaxial mechanical response of porcine tricuspid valve leaflets, Journal of Biomechanical Engineering 138 (10) (2016) 104504.

[32]. Pham T, Sulejmani F, Shin E, Wang D, Sun W, Quantification and comparison of the mechanical properties of four human cardiac valves, Acta Biomaterialia 54 (2017) 345–355. [PubMed: 28336153]

[33]. Jett S, Laurence D, Kunkel R, Babu AR, Kramer K, Baumwart R, Towner R, Wu Y, Lee C-H, An investigation of the anisotropic mechanical properties and anatomical structure of porcine atrioventricular heart valves, Journal of the Mechanical Behavior of Biomedical Materials 87 (2018) 155–171. [PubMed: 30071486]

[34]. Pokutta-Paskaleva A, Sulejmani F, DelRocini M, Sun W, Comparative mechanical, morphological, and microstructural characterization of porcine mitral and tricuspid leaflets and chordae tendineae, Acta Biomaterialia 85 (2019) 241–252. [PubMed: 30579963]

[35]. Sacks MS, Biaxial mechanical evaluation of planar biological materials, Journal of Elasticity 61 (1-3) (2000) 199–246.

[36]. Pant AD, Thomas VS, Black AL, Verba T, Lesicko JG, Amini R, Pressure-induced microstructural changes in porcine tricuspid valve leaflets, Acta Biomaterialia 67 (2018) 248–258. [PubMed: 29199067]

[37]. Balachandran K, Alford PW, Wylie-Sears J, Goss JA, Grosberg A, Bischoff J, Aikawa E, Levine RA, Parker KK, Cyclic strain induces dual-mode endothelial-mesenchymal transformation of the cardiac valve, Proceedings of the National Academy of Sciences 108 (50) (2011) 19943–19948.

[38]. Khang A, Buchanan RM, Ayoub S, Rego BV, Lee C-H, Ferrari G, Anseth KS, Sacks MS, Mechanobiology of the heart valve interstitial cell: Simulation, experiment, and discovery, in: Mechanobiology in Health and Disease, Elsevier, 2018, pp. 249–283.

[39]. Mangieri A, Montalto C, Pagnesi M, Jabbour RJ, Rodés-Cabau J, Moat N, Colombo A, Latib A, Mechanism and implications of the tricuspid regurgitation, Circulation: Cardiovascular Interventions 10 (7).

[40]. Di Mauro M, Bivona A, Iaco AL, Contini M, Gagliardi M, Varone E, Gallina S, Calafiore AM, Mitral valve surgery for functional mitral regurgitation: prognostic role of tricuspid regurgitation, European Journal of Cardio-Thoracic Surgery 35 (4) (2009) 635–640. [PubMed: 19233670]

[41]. Taramasso M, Vanermen H, Maisano F, Guidotti A, La Canna G, Alfieri O, The growing clinical importance of secondary tricuspid regurgitation, Journal of the American College of Cardiology 59 (8) (2012) 703–710. [PubMed: 22340261]

[42]. Martin C, Sun W, Biomechanical characterization of aortic valve tissue in humans and common animal models, Journal of Biomedical Materials Research Part A 100A (6) (2012) 1591–1599.

[43]. Meador WD, Sugerman GP, Story HM, Seifert AW, Bersi MR, Tepole AB, Rausch MK, The regional-dependent biaxial behavior of young and aged mouse skin: A detailed histomechanical characterization, residual strain analysis, and constitutive model, Acta Biomaterialia.

[44]. Dudziak M, Skwarek M, Hreczecha J, Jerzemowski J, Grzybiak M, Microscopic study of right fibrous annulus, Folia Morphologica 68 (1) (2009) 32–35. [PubMed: 19384827]

[45]. Messer S, Moseley E, Marinescu M, Freeman C, Goddard M, Nair S, Histologic analysis of the right atrioventricular junction in the adult human heart., The Journal of heart valve disease 21 (3) (2012) 368–73. [PubMed: 22808841]

[46]. Basu A, Lacerda C, He Z, Mechanical properties and composition of the basal leaflet-annulus region of the tricuspid valve, Cardiovascular Engineering and Technology 9 (2) (2018) 217–225. [PubMed: 29484539]

[47]. Gosline J, Lillie M, Carrington E, Guerette P, Ortlepp C, Savage K, Elastic proteins: Biological roles and mechanical properties, Philosophical Transactions of the Royal Society of London. Series B: Biological Sciences 357 (1418) (2002) 121–132. [PubMed: 11911769]

[48]. Sacks MS, David Merryman W, Schmidt DE, On the biomechanics of heart valve function, Journal of Biomechanics 42 (12) (2009) 1804–1824. [PubMed: 19540499]

[49]. Grande-Allen KJ, Glycosaminoglycans and proteoglycans in normal mitral valve leaflets and chordae: association with regions of tensile and compressive loading, Glycobiology 14 (7) (2004) 621–633. [PubMed: 15044391]

[50]. Malinowski M, Jazwiec T, Goehler M, Quay N, Bush J, Jovinge S, Rausch MK, Timek TA, Sonomicrometry-derived 3-dimensional geometry of the human tricuspid annulus, The Journal of Thoracic and Cardiovascular Surgery 157 (4) (2019) 1452–1461.e1. [PubMed: 30392947]

[51]. Rausch MK, Malinowski M, Wilton P, Khaghani A, Timek TA, Engineering analysis of tricuspid annular dynamics in the beating ovine heart, Annals of Biomedical Engineering 46 (3) (2018) 443–451. [PubMed: 29139013]

[52]. Balachandran K, Konduri S, Sucosky P, Jo H, Yoganathan AP, An ex vivo study of the biological properties of porcine aortic valves in response to circumferential cyclic stretch, Annals of Biomedical Engineering 34 (11) (2006) 1655–1665.

[53]. Stephens EH, Timek TA, Daughters GT, Kuo JJ, Patton AM, Baggett LS, Ingels NB, Miller DC, Grande-Allen KJ, Significant changes in mitral valve leaflet matrix composition and turnover with tachycardia-induced cardiomyopathy, Circulation 120 (SUPPL. 1) (2009) S112–9. [PubMed: 19752355]

[54]. Icardo JM, Colvee E, Revuelta JM, Structural analysis of chordae tendineae in degenerative disease of the mitral valve, International Journal of Cardiology 167 (4) (2013) 1603–1609. [PubMed: 22564390]

[55]. Ayoub S, Lee C-H, Driesbaugh KH, Anselmo W, Hughes CT, Ferrari G, Gorman RC, Gorman JH, Sacks MS, Regulation of valve interstitial cell homeostasis by mechanical deformation: implications for heart valve disease and surgical repair, Journal of The Royal Society Interface 14 (135) (2017) 20170580.

[56]. Gupta V, Grande-Allen KJ, Effects of static and cyclic loading in regulating extracellular matrix synthesis by cardiovascular cells, Cardiovascular Research 72 (3) (2006) 375–383. [PubMed: 17010955]

[57]. Gheorghe L, Rensing BJ, Van der Heyden JA, Eefting FD, Post MC, Rana B, Swaans MJ, Transcatheter Tricuspid Valve Interventions: An Emerging Field, Current Cardiology Reports 21 (5) (2019) 1–10. [PubMed: 30631962]

[58]. Stuge O, Liddicoat J, Emerging opportunities for cardiac surgeons within structural heart disease, Journal of Thoracic and Cardiovascular Surgery 132 (6) (2006) 1258–1261. [PubMed: 17140937]

[59]. Fehervary H, Vander Sloten J, Famaey N, Development of an improved parameter fitting method for planar biaxial testing using rakes, International Journal for Numerical Methods in Biomedical Engineering 35 (4) (2019) 1–17.

[60]. Wafae N, Hayashi H, Gerola LR, Vieira MC, Anatomical study of the human tricuspid valve., Surgical and radiologic anatomy : SRA 12 (1) (1990) 37–41. [PubMed: 2345895]

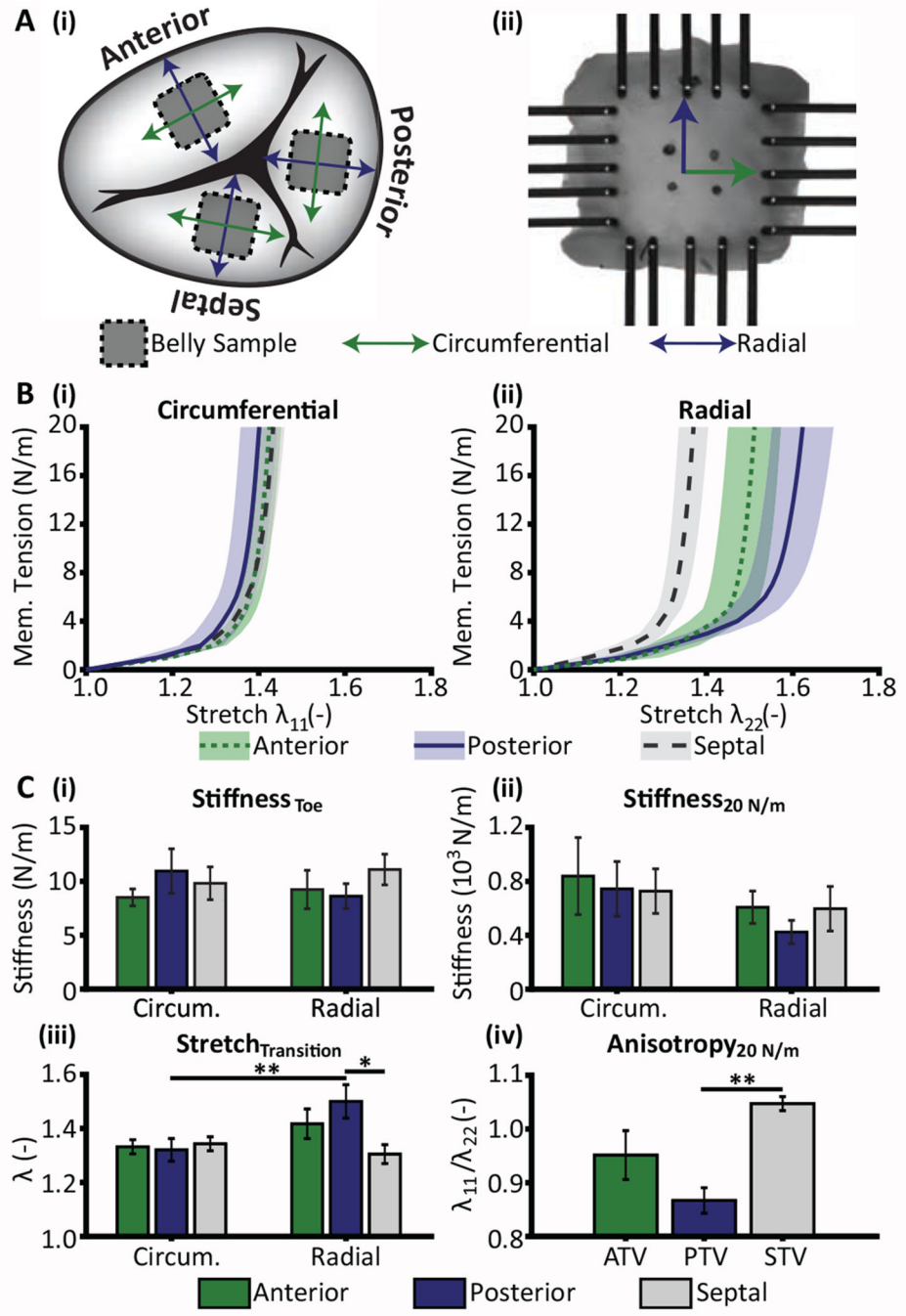

Figure 1:

The tricuspid leaflets exhibit varying degrees of mechanical anisotropy. (A) (i) Schematic showing tissue samples from the belly region of anterior, posterior, and septal leaflets that were (ii) mounted in alignment with the circumferential and radial directions and tested under biaxial tension. (B) Equibiaxial membrane tension and stretch response of anterior, posterior and septal leaflets in (i) circumferential and (ii) radial directions. (C) Quantification of (i) toe region, (ii) 20 N/m stiffness, (iii) transition stretch representing the stretch at which collagen becomes engaged, and (iv) mechanical anisotropy index calculated

as the ratios between circumferential and radial stretch at 20 N/m. Data in all plots reported as mean ± SEM ($n = 6$ per leaflet, $*p < 0.05$, $* * p < 0.01$)

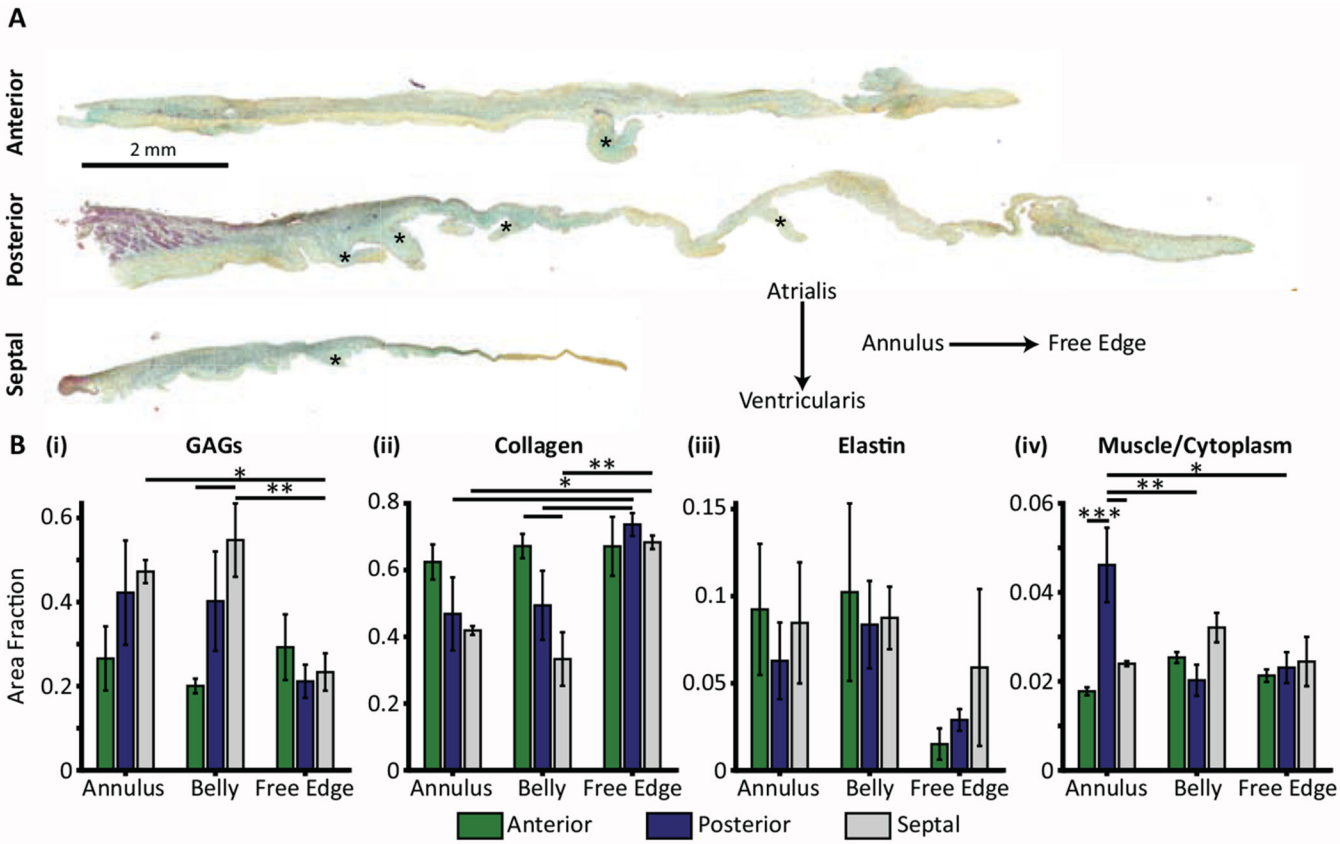

Figure 2:

Leaflet histology reveals that collagen content and glycosaminoglycan content vary by leaflet and region.(A) Images of representative Movat's Pentachrome stained radial strips of anterior, posterior, and septal leaflets (scale bar = 2 mm). Black asterisks denote the sites of chordae tendineae attachments excluded from analysis. (B) Quantification of leaflet constituent area fractions for (i) glycosaminoglycans (GAGs), (ii) collagen, (iii) elastin, and (iv) muscle/cytoplasm, at the annulus (i.e., first third of strip), belly (i.e., middle third of strip), and free edge (i.e., last third of strip). All data presented as mean ± SEM. Leaflet images as shown were white balanced. (n = 3 subjects, 2 images per region averaged per leaflet, *$p < 0.05$, * * $p < 0.01$, * * *$p < 0.001$)

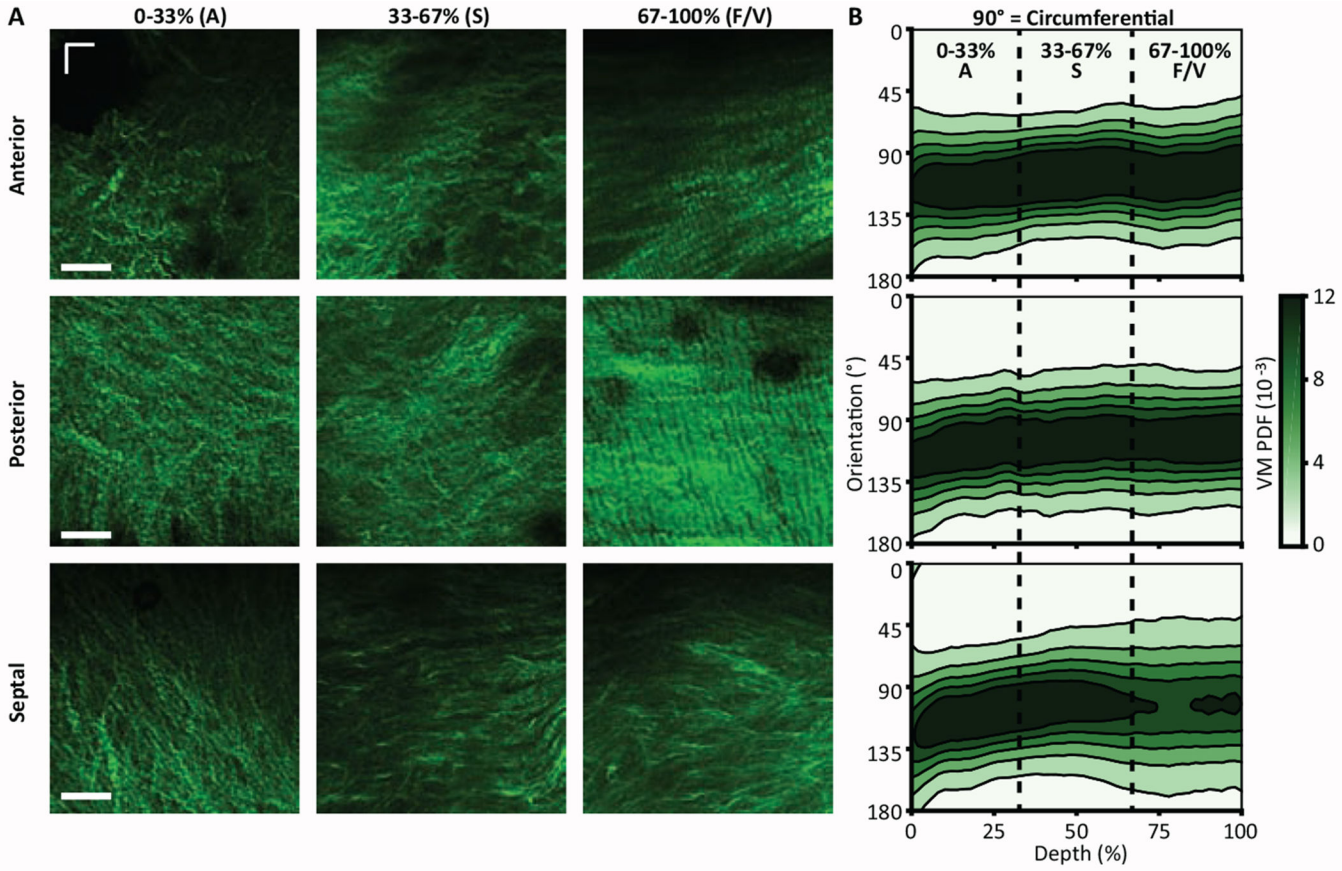

Figure 3:

Second harmonic generation analysis of collagen orientation reveals orientation variation among leaflets and depth in the belly. (A) Representative collagen images (green) from depths of 0-33% (Atrialis), 33-67% (Spongiosa), and 67-100% (Fibrosa/Ventricularis) for anterior, posterior, and septal leaflets. Circumferential direction aligns horizontally and radial direction aligns vertically (scale bar = 100 μm). For each sample, we imaged 500x500 μm z-stacks at three locations in the center of the sample with step sizes of 10 μm. (B) Von Mises probability distribution functions representing collagen orientation mean and concentration by depth for anterior, posterior, and septal leaflets, respectively. Note, distribution functions were created by averaging data across animals and across sample locations within one depth. Orientations of 90° align with the circumferential direction. Vertical hashed lines indicate summary regions for statistical comparison. Important Note: Image intensity in (A) was enhanced to improve visualization of fiber orientations, and should not be interpreted as correlating with quantity of collagen. (n = 6 per leaflet)

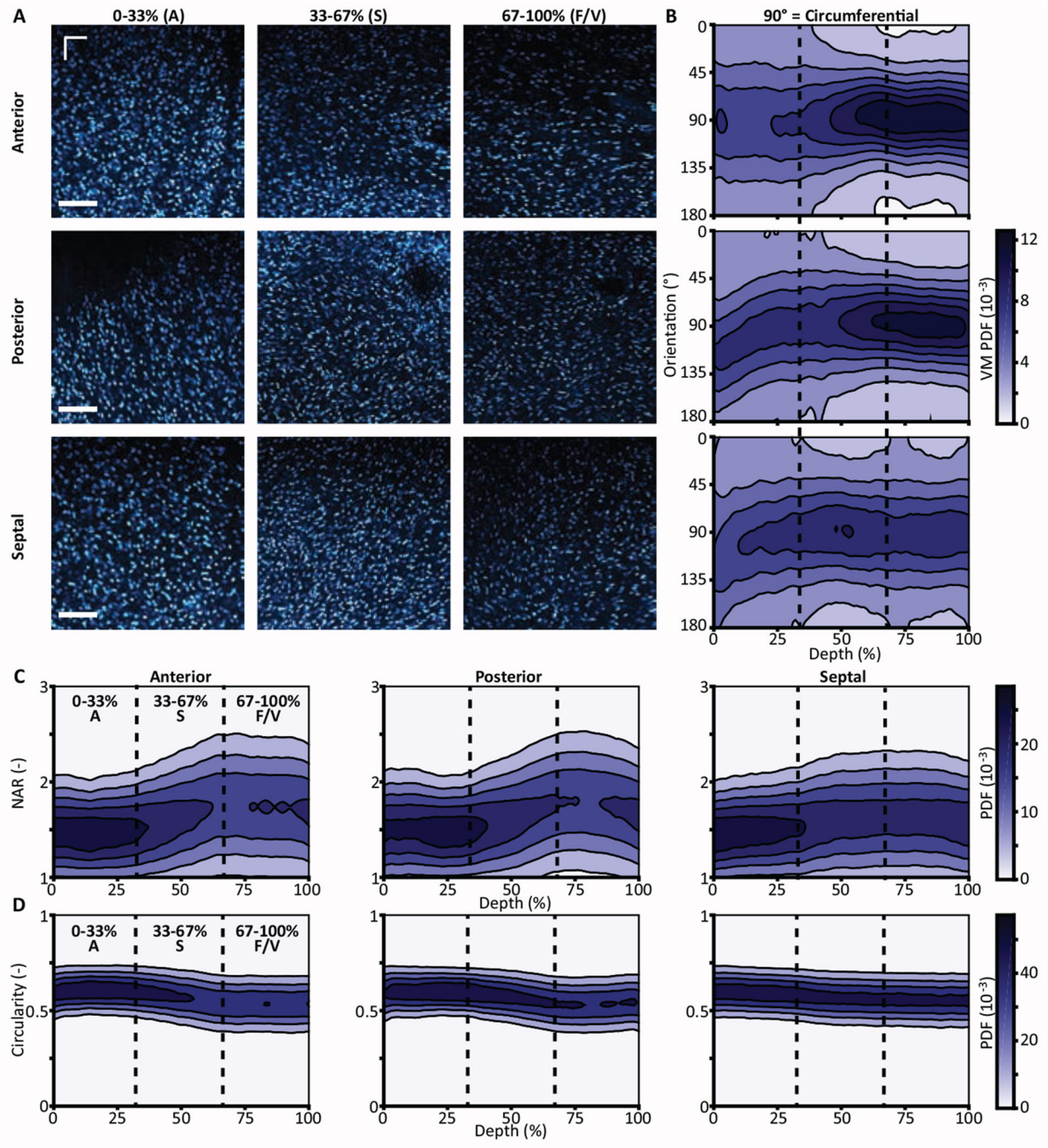

Figure 4:

Valvular interstitial cell nuclei orientation aligns with collagen orientation. (A) Representative nuclei images (cyan) at depths 0-33% (Atrialis), 33-67% (Spongiosa), and 67-100% (Fibrosa/Ventricularis) for anterior, posterior, and septal leaflets. Circumferential direction aligns horizontally and radial direction aligns vertically (scale bar = 100 μm). (B) Von Mises probability distribution functions visualizing nuclei orientation mean and concentration by depth for anterior, posterior, and septal leaflets. Orientations of 90° align with the circumferential direction . (C-D) Normal probability distribution functions

visualizing (C) nuclear aspect ratio and (D) nuclear circularity by depth for anterior, posterior, and septal leaflets. Vertical hashed lines indicate summary regions for statistical comparison. Important Note: Image intensity in (A) was enhanced to improve visualization of nuclei morphology. As such, fluorescence intensity should not be interpreted quantitatively. (n = 6 per leaflet)

Table 1:

Von Mises parameters for average collagen orientation distributions throughout the depth of anterior, posterior, and septal leaflets. Parameters μ and κ represent the fiber orientation mean and concentration, respectively. Circumferential direction aligns with 90°.

Collagen Orientation						
Depth: (%)	**Anterior**		**Posterior**		**Septal**	
	μ(°)	κ(−)	μ(°)	κ(−)	μ(°)	κ(−)
0	117.7	1.09	119.3	1.33	126.0	0.92
10	114.5	1.51	112.1	1.66	113.7	1.54
20	113.3	1.48	110.3	1.77	110.9	1.54
30	111.1	1.73	106.7	1.74	105.8	1.61
40	107.2	1.93	107.6	1.63	102.5	1.53
50	106.2	1.96	105.5	1.64	100.4	1.37
60	103.3	1.69	104.3	1.60	102.5	1.20
70	106.1	1.60	106.9	1.46	103.8	1.03
80	107.5	1.60	108.1	1.62	103.8	0.98
90	105.8	1.51	107.4	1.81	103.1	1.06
100	100.3	1.50	105.2	1.68	102.3	1.01

Note: Larger κ values indicate a larger concentration of fiber orientations in mean direction

Table 2:

Von Mises parameters of average nuclei orientation distributions, and average normal distribution parameters for nuclear aspect ratio and nuclei circularity for anterior, posterior, and septal leaflets. Von Mises distribution parameters μ and κ represent the mean nuclei orientation and concentration, respectively. Normal distribution parameters μ and σ represent the mean values and standard deviations, respectively. Circumferential direction aligns with 90°.

Nuclei Orientation

Depth: (%)	Anterior		Posterior		Septal	
	μ(°)	κ(−)	μ(°)	κ(−)	μ(°)	κ(−)
0	89.5	0.35	116.7	0.42	124.5	0.17
10	92.6	0.37	106.9	0.47	102.8	0.39
20	91.3	0.37	94.0	0.51	94.6	0.44
30	93.7	0.42	90.6	0.50	89.8	0.49
40	90.3	0.53	88.1	0.50	88.6	0.56
50	88.7	0.73	86.1	0.64	87.1	0.62
60	84.6	0.95	85.7	0.84	91.1	0.60
70	87.1	1.10	85.6	0.93	92.1	0.49
80	88.6	1.05	88.9	1.00	91.9	0.53
90	87.2	1.05	90.1	0.97	92.3	0.59
100	91.2	0.92	92.0	0.81	91.3	0.50

Nuclear Aspect Ratio

Depth: (%)	Anterior		Posterior		Septal	
	μ(−)	σ(−)	μ(−)	σ(−)	μ(−)	σ(−)
0	1.47	0.32	1.49	0.34	1.44	0.30
10	1.45	0.31	1.51	0.34	1.47	0.31
20	1.46	0.32	1.48	0.32	1.49	0.33
30	1.49	0.34	1.48	0.32	1.52	0.35
40	1.54	0.37	1.54	0.36	1.56	0.37
50	1.63	0.41	1.60	0.39	1.61	0.40
60	1.72	0.44	1.70	0.42	1.61	0.40
70	1.76	0.45	1.79	0.43	1.63	0.40
80	1.75	0.44	1.79	0.44	1.63	0.40
90	1.73	0.44	1.75	0.43	1.61	0.39
100	1.68	0.42	1.65	0.41	1.56	0.37

Nuclei Circularity

Depth: (%)	Anterior		Posterior		Septal	
	μ(−)	σ(−)	μ(−)	σ(−)	μ(−)	σ(−)
0	0.59	0.08	0.59	0.09	0.60	0.08
10	0.60	0.07	0.60	0.08	0.60	0.08
20	0.61	0.07	0.60	0.07	0.59	0.08

Nuclei Orientation						
Depth: (%)	**Anterior**		**Posterior**		**Septal**	
	***μ*(°)**	**$\hat{\kappa}$(−)**	***μ*(°)**	**$\hat{\kappa}$(−)**	***μ*(°)**	**$\hat{\kappa}$(−)**
30	0.60	0.08	0.60	0.07	0.58	0.08
40	0.59	0.08	0.58	0.08	0.57	0.08
50	0.57	0.08	0.57	0.08	0.56	0.08
60	0.55	0.09	0.55	0.08	0.56	0.08
70	0.53	0.09	0.53	0.09	0.56	0.08
80	0.54	0.09	0.53	0.09	0.56	0.08
90	0.53	0.09	0.54	0.09	0.55	0.08
100	0.54	0.09	0.54	0.09	0.55	0.08

Note: Larger $\hat{\kappa}$ values indicate more concentrated nuclei orientations in mean direction